On the activity of the redox couple peroxide/oxide ion: case study of $Ba_5Ru_2O_{11}$ in aqueous and organic solvents

Alexis Grimaud,[1,2]* Antonella Iadecola,[2] Dmitry Batuk,[1,3] Mathieu Saubanère,[2,4] Artem M. Abakumov,[3] John W. Freeland,[5] Jordi Cabana,[6] Haifeng, Li,[6] Marie-Liesse Doublet,[2,4] Gwenaëlle Rousse[1,2,7] and Jean-Marie Tarascon[1,2,7,8].

1 - Chimie du Solide et de l'Energie, UMR 8260, Collège de France, 75231, Paris Cedex 05, France
2 - Réseau sur le Stockage Electrochimique de l'Energie (RS2E), CNRS FR 3459,33 rue Saint Leu, 80039, Amiens Cedex, France
3 - EMAT, University of Antwerp, Groenenborgerlaan 171, 2020, Belgium
4 - Institut Charles Gerhardt, CNRS UMR 5253, Université Montpellier, Place E. Bataillon, 34095 Montpellier, France
5 - Advanced Photon Source, Argonne National Laboratory, Argonne, IL 60439, USA
6 - Department of Chemistry, University of Illinois at Chicago, Chicago, Illinois 60607, United States
7 - Joint Center for Energy Storage Research (JCESR), Argonne National Laboratory, Lemont, Illinois 60439, United States
8 - Sorbonne Universités - UPMC Université Paris 06, Paris, France
9 - ALISTORE-European Research Institute, Amiens, France

Corresponding Author:
* E-mails: alexis.grimaud@college-de-france.fr

Abstract:

The finding that triggering the redox activity of oxygen ions within the lattice of transition metal oxides for boosting the performances of materials used in energy storage and conversion devices such Li-ion batteries or oxygen evolution electrocatalysts has recently attracted attention. While experimental and theoretical works have been critical to understand the role of oxygen non-bonding states for triggering the redox activity of oxygen ions, the field currently lacks knowledge about the redox chemistry of oxygen species formed upon this oxidation process. This can be in part explained by the complexity to stabilize and study these species when electrochemically formed. In this work, we alleviate this difficulty by studying the phase $Ba_5Ru_2O_{11}$ which contains true peroxide O_2^{2-} groups as oxygen evolution reaction electrocatalysts and Li-ion battery materials. Combining physical characterizations and electrochemical measurements, we could demonstrate that peroxide groups can easily be oxidized at relatively low potential, leading to the formation of gaseous oxygen and triggering the instability of the oxide. Furthermore, we demonstrate that owing from the stabilization at high energy of empty σ^* antibonding O-O states for the peroxide, limited reversibility of electrochemical reactions when the O_2^{2-}/O^{2-} redox couple is used as redox center for Li-ion battery materials or as OER redox active sites is foreseen. Overall, this work suggests that the formation of true peroxide O_2^{2-} states are detrimental for transition metal oxides used as OER catalysts and Li-ion battery materials. Rather, oxygen species with O-O bond order lower than 1 would be preferred for these applications.

Introduction

The deployment of renewable energies is arguably one of the major challenges faced by humankind, which will only be achieved by the development of efficient energy storage devices. Electrochemical devices such as batteries, supercapacitors or electrolyzers will certainly take a major role in the energy storage, provided that cost-effective and earth abundant materials can be developed in order to master the complex electrochemical reactions happening at the electrodes.[1–3] The fields of batteries and electrocatalysis were so far regarded as antagonists since the former is governed by thermodynamically-driven bulk processes while the latter is controlled by kinetics on the surface of materials. Nevertheless, they recently became closer, owing to the realization that mastering the redox chemistry of oxygen ions is at the heart of the development of both energy-dense Li-rich layered compounds for Li-ion battery materials and better oxygen evolution reaction (OER) catalysts.[4–8]

The quest for mastering the redox chemistry of oxide ions in transition metal oxides has significantly advanced the understanding of the field (Figure 1). For Li-rich layered compounds, theoretical and experimental works pointed towards the importance of accessing the energy level of non-bonding 2p oxygen states. Upon oxidation lattice oxygen ions O^{2-} can form O-O bonds and the so-called peroxo-like species $(O_2)^{n-}$ that are characterized by a relatively short O-O distances with a low bond order (lower than 1) and the formation of new energy states.[5,9–13] This reversible process occurs at potential lower than about 4.3 V vs. Li^+/Li. When pushing above this potential, which corresponds to the standard potential $E°(O_2/H_2O)$ at pH = 0, the direct four electron formation of gaseous oxygen can occur through the condensation of O-O states within the lattice of the transition

metal oxide. The correspondence between both phenomena can be rationalized assuming a similar chemical potential of oxide ions in the bulk of the transition metal oxide and in water (a similar assumption is made when considering the chemical potential of lithium inside the insertion electrode and in metallic lithium which is used as reference for thermodynamical calculations). This similarity is further exemplified when noting that bulk oxygen release was observed for Mn^{4+}-based Li_2MnO_3.[9,14,15] Indeed, for both Mn^{4+}-based oxygen evolving center (OEC),[16] cofactor of the Photosystem II (PSII) which naturally oxidizes water to evolve oxygen, and Li_2MnO_3 no Mn^{5+} was observed upon oxidation. Rather, for the OEC the oxidation of water occurs through the formation of oxidized oxygen radicals.[17] More striking is the similar O-O bond distance of about 2.1 - 2.4 Å found for these Mn-based oxides upon oxidation and the oxyl-oxo bond formation for the cofactor.[18–20] Besides, similar O-O bond formation occurs for Ru-based compounds used as homogeneous OER catalysts and Li-ion battery materials.[5,21] This relatively large O-O bond distance indicates a low bond order and the formation of a peroxo-like $(O_2)^{n-}$ species with n being close to 3 upon one electron removal, rather than true peroxide $(O_2)^{2-}$ species.

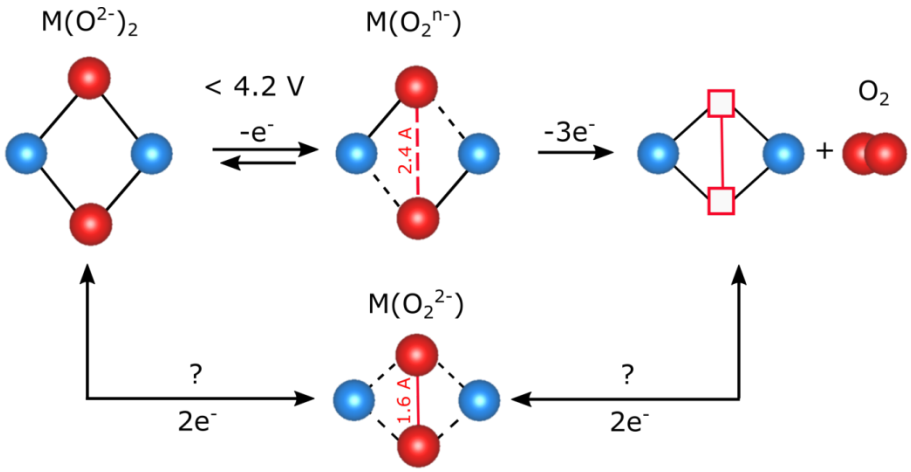

Figure 1: Schematic representation of the oxygen redox chemistry in transition metal oxides with the transition from oxide ion (O^{2-}) to peroxo-like $(O_2)^{n-}$ groups, peroxide $(O_2)^{2-}$ all the way to gaseous oxygen release.

Overall, a central question for mastering the redox activity of oxygen for the fields of batteries and electrocatalysts concerns the O-O bond formation that can either occur through the coupling of two lattice oxygen ions (mechanism poised as direct-coupling by the electrocatalysis community) or through the reaction of one oxidized oxygen ions (also called oxyl radical) with water or carbonate solvent molecules acting as nucleophilic species (mechanism defined as acid-base).[22,23] Evidences for both mechanisms were found for layered compounds used as Li-ion battery electrodes[5,24–28] as well as for transition metal oxides used as heterogeneous OER catalysts,[29–34] while the Mn-based cofactor of PSII is believed to evolve oxygen through a direct-coupling mechanism.[19] Nevertheless, questions still remain about the exact chemical and electronic nature of these O-O bonds and the stability of these intermediate species towards condensation and oxygen release. Hence, only a full understanding of them will allow for developing better battery materials as well as catalysts for the OER.

Driven by these questions, we decided to study the redox behavior of O-O bonds in the bulk of transition metal oxides, but only a very few oxides were reported so far to contain true peroxide groups. Among them is the family of hexagonal perovskites with the compounds $La_{1.2}Sr_{2.7}MO_{7.33}$, $La_2Sr_2PtO_{7+\delta}$ or $Ba_5Ru_2O_{11}$.[35–37] In this work, we selected $Ba_5Ru_2O_{11}$ as a model compound owing to its similarities with the well-studied Ru-based oxides used as battery electrode materials and OER catalysts. More specifically, we studied the redox chemistry of bulk peroxide groups pertaining to $Ba_5Ru_2O_{11}$ by combining a physical and an electrochemical study in both aqueous and aprotic media.

Results and discussion

The structure of the hexagonal perovskite $Ba_5Ru_2O_{11}$ was previously reported by Darriet et al.[37] It is built on the alternating stacking of three BaO_3 and one Ba_2O_2 layers, where Ru occupies octahedral sites forming face-sharing Ru_2O_9 dimers along [001] (Fig. 2a). The peroxide groups O_2^{2-} are located in the Ba_2O_2 layers and are statistically distributed among three possible configurations due to the thermal entropy (Fig. 2b). The structure of a reduced phase (e.g; oxygen deficient) $Ba_5Ru_2O_{10}$ shows the same symmetry and similar Ba-Ru framework as the parent compound,[38] in which the $(O_2)^{2-}$ peroxide species are replaced by a single oxygen atom located at the origin of the cell (Fig. 2c). Therefore, we first confirmed that our sample is phase pure, by means of laboratory X-ray diffraction (XRD). The XRD pattern can be indexed using the *P* $6_3/m$ *m c* hexagonal space group with lattice parameters *a* = 5.95144(9) Å and *c* = 18.0537(3) Å. These lattice parameters are in line with those reported for $Ba_5Ru_2O_{11}$ and expected to be larger than those for $Ba_5Ru_2O_{10}$. However, the use of XRD doesn't allow for distinguishing between the $Ba_5Ru_2O_{10}$ and the $Ba_5Ru_2O_{11}$ structures as refinements performed with both structural models give equally good results. Therefore, the structure was refined using neutron powder diffraction (NPD), which is much more sensitive to oxygen than X-rays. The NPD patterns collected at two different wavelengths (λ = 1.29 Å and 2.53 Å) were simultaneously refined by the Rietveld method, using either the $Ba_5Ru_2O_{10}$ structural model where one oxygen fully occupies the 2*a* (0,0,0) position, or the $Ba_5Ru_2O_{11}$ model, in which the 2*a* oxygen is displaced to the 12*k* (*x*, 2*x*, *z*) position with a partial occupancy of 1/3, so as to form peroxide $(O_2)^{2-}$ groups statistically distributed around the *c*-axis (Fig. 2b). The fit using the $Ba_5Ru_2O_{10}$ model results in wrong relative intensities for the (004)/(102) doublet and leads to an unrealistic thermal parameter B_{iso} of 15 Å² for the oxygen atom in 2*a* position (Fig. 3a and Table 1). In contrary, the

refinement using the $Ba_5Ru_2O_{11}$ model gives a very good fit as seen in Fig. 3b, confirming the formation of true peroxide $(O_2)^{2-}$ groups within the lattice of $Ba_5Ru_2O_{11}$. The final atomic positions are reported in Table 1 giving the O-O bond length of 1.617 Å for the peroxide groups.

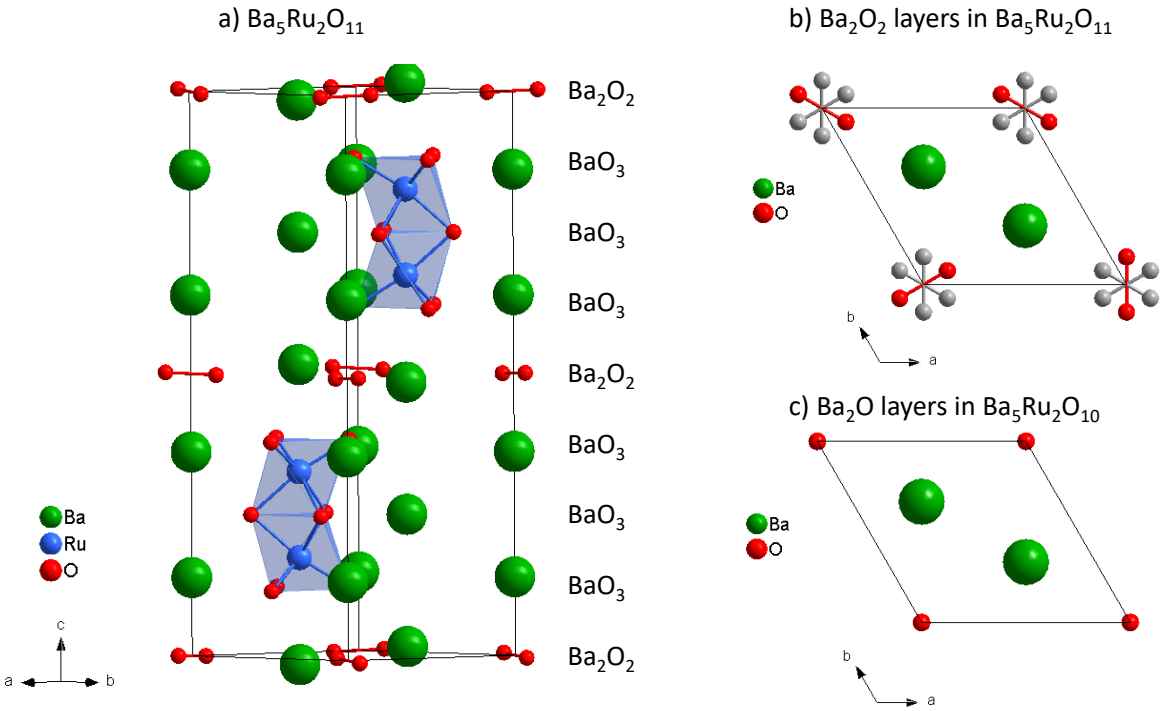

Figure 2: a. Structure of $Ba_5Ru_2O_{11}$ showing alternance of BaO_3 layers and Ba_2O_2 layers. **b.** Peroxo groups in Ba_2O_2 layers are statistically distributed over three possible configurations (shown in gray) and a possible configuration is shown in red. **c.** shows the Ba_2O layers that replace the Ba_2O_2 layers to form $Ba_5Ru_2O_{10}$.

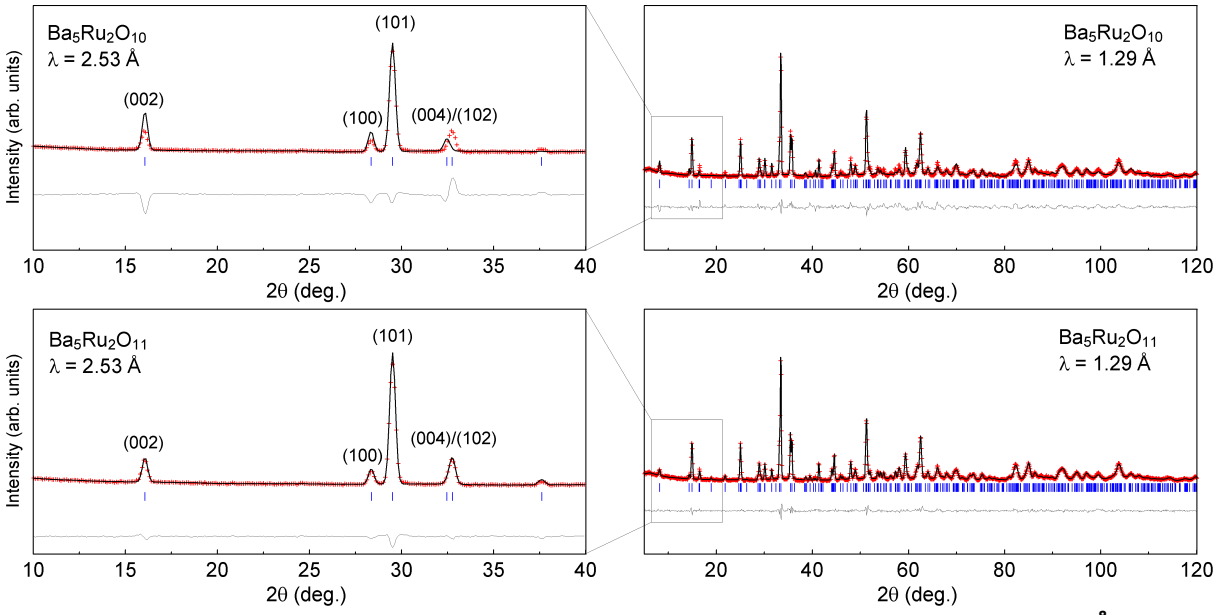

Figure 3: Rietveld refinement of the neutron diffraction patterns recorded with λ = 1.29 Å and λ = 2.53 Å. The top panel shows the refinement obtained from the $Ba_5Ru_2O_{10}$ structural model while the bottom one is performed from the $Ba_5Ru_2O_{11}$ model. The red crosses, black continuous line and bottom green line represent the observed, calculated, and difference patterns, respectively. Vertical blue tick bars mark the reflection positions.

Table 1. Structural parameters for $Ba_5Ru_2O_{11}$, deduced from the combined Rietveld refinement of the neutron diffraction patterns recorded with λ = 1.29 Å and λ = 2.53 Å at 300K.

$Ba_5Ru_2O_{11}$; Space Group: *P* $6_3/m$ *m c*

a = 5.9562(2) Å, *c* = 18.0779(8) Å, *V* = 555.41(4) $Å^3$

Atom	**Wyckoff site**	***x***	***y***	***z***	**B($Å^2$)**	**Occ**
Ba1	4*e*	0	0	0.1389(4)	0.22(13)	1
Ba2	2*c*	1/3	2/3	1/4	0.05(18)	1
Ba3	4*f*	1/3	2/3	0.0158(4)	1.14(16)	1
Ru1	4*f*	1/3	2/3	0.6738(2)	0.28(9)	1
O1	6*h*	0.1842(9)	0.3684(9)	3/4	0.80(10)	1
O2	12*k*	0.4901(6)	0.9802(6)	0.61806(19)	0.83(6)	1
O3	12*k*	0.0782(10)	0.1565(10)	-0.0024(9)	0.9(3)	1/3

dataset λ = 1.29 Å: Bragg R-factor= 6.19%, Rf-factor= 4.65%;

dataset λ = 2.53 Å: Bragg R-factor= 3.57%, Rf-factor= 3.52%

Scanning transmission electron microscopy (STEM) was employed to analyze the local oxygen coordination environment in the structure. Complementary high angle annular dark-field and annular bright field STEM (HAADF-STEM and ABF-STEM) images of the material along the [$10\bar{1}0$] direction are shown in Figs. 4a,b. The HAADF-STEM images highlight projected positions of the heavy atomic columns, i.e. Ru and Ba, while the ABF-STEM images also contain signal from the light O columns. The HAADF-STEM image confirms the cationic arrangement of the material, corresponding to the layered 2H hexagonal perovskite type structure. In the image, BaO and Ru columns inside the perovskite blocks form characteristic chevron pattern on three BaO (slightly brighter) and two Ru columns. The perovskite blocks are separated by planar interfaces of double Ba column, corresponding to the Ba_2O_2 layers. In the ABF-STEM image, O columns inside the perovskite blocks produce sharp well defined spots next to the Ru columns, while the O signal in the Ba_2O_2 layers is less pronounced. According to the theoretical ABF-STEM images (Figs. 4d,f), the difference between the $Ba_5Ru_2O_{11}$ and $Ba_5Ru_2O_{10}$ models is very subtle and pertains to the intensity of the O signal in the Ba_2O_2 layers. While the simulations for both models reproduce well the overall appearance of the experimental images, neither of them is a direct match. A close comparison of the experimental and the theoretical HAADF-STEM and ABF-STEM images reveal two major differences: 1) in the experimental images projected Ba columns in the Ba_2O_2 layers are somewhat smeared in the (001) plane compared to those in the perovskite blocks and 2) the intensity of the O columns in the experimental ABF-STEM is not exactly centered in-between the Ba columns. Taking into account that the signal from light atomic columns in ABF-STEM images is very sensitive to the long range ordering of the structure,[39] these discrepancies indicate that the peroxo-like species in the Ba_2O_2 layered are either statistically distributed or dynamic. Either way, these static/dynamic O displacements

apparently also affects the adjacent Ba positions, which is consistent with the crystal structure analysis using NPD data, showing elevated thermal displacement parameter for the corresponding Ba3 positions (Table 1).

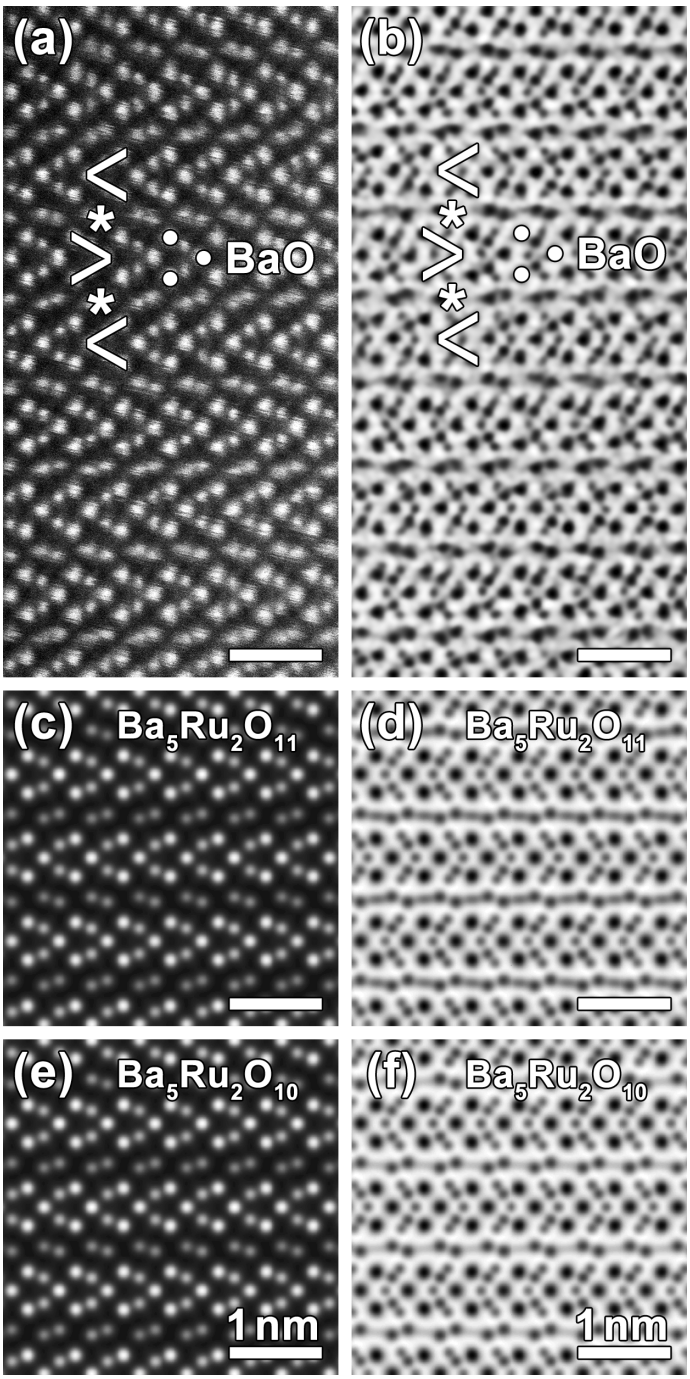

Figure 4: Experimental [10$\bar{1}$0] HAADF-STEM (a) and ABF-STEM (b) images of the pristine $Ba_5Ru_2O_{11}$ compound investigated in this work, together with theoretical images calculated using structure model for the $Ba_5Ru_2O_{11}$ (c,d) and $Ba_5Ru_2O_{10}$ (e,f) compounds. In the

experimental images, perovskite blocks are highlighted with chevrons made up of 3 BaO (marked with circles) and 2 Ru columns; the Ba_2O_2 layers between the perovskite blocks are marked with asterisks. Note the presence of additional dots in ABF-STEM images (compared to HAADF-STEM) next to the Ru columns, corresponding to the O columns. Together with the O atoms in the BaO these O positions form projection of the RuO_6 octahedra.

Following this structural study, we analyzed the electronic signature of the peroxo-groups by means of X-ray absorption spectroscopy (XAS), Raman spectroscopy and density functional theory (DFT) calculation. X-ray absorption near edge structure (XANES) measurements at the Ru K-edge (Fig. 5a) confirmed ruthenium to be in an oxidation state of 5+ by comparing the edge position with $Li_2Ru^{4+}O_3$, $Li_3Ru^{5+}O_4$, $La_2LiRu^{5+}O_6$ and $Na_2Ru^{6+}O_6$ reference compounds. Furthermore, the appearance of a small pre-edge peak at about 22120 eV reveals the non-centrosymmetric position of ruthenium atom in the RuO_6 octahedra (Fig. 5b), as already observed for Li_3RuO_4,[40] due to the short distances between the centers of the octahedra sharing faces. This is confirmed by the analysis of the extended x-ray absorption fine structure (EXAFS) oscillations (Fig. 5b). Then, using Raman spectroscopy, a vibration at about 800 cm^{-1} characteristic of O-O bond stretching[41] was found for the pristine compound (Fig. S1). Finally, DFT calculations were carried out using the structure of $Ba_5Ru_2O_{11}$ refined by NPD (Fig. 5). The atom-projected density of states (pDOS) shows RuO* states above the Fermi level with a predominant Ru character (Fig. 6a). This is confirmed when plotting the negative Fukui function, which reveals that the states involved in the reduction (electron addition) are t_{2g}-like local level (Fig. 6b). Below the Fermi level, pDOS evidences a predominant oxygen character with O(*p*) states being even greater than Ru(*d*) states, indicating that in addition to the RuO* states, non-bonding oxygen states may lie below the Fermi level as previously discussed for other Ru-based compounds.[9,42] Furthermore, pDOS

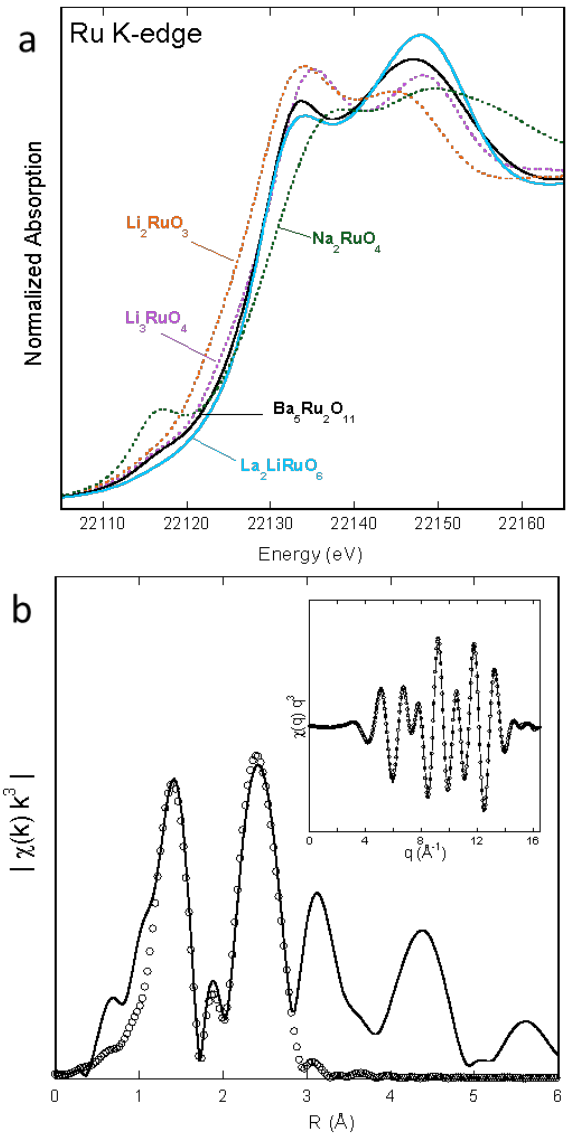

Figure 5: **a** Ru K-edge XANES spectra of $Ba_5Ru_2O_{11}$ compared to Ru^{5+}-containing perovskite La_2LiRuO_6, Ru^{5+}-containing rock salt Li_3RuO_4 and Ru^{4+}-containing layered compound Li_2RuO_3 and **b** Magnitude of Fourier transform (FT) of k^3-weighted EXAFS oscillations (solid line) of $Ba_5Ru_2O_{11}$ along with fitting results (open circles). In inset shows the filtered EXAFS oscillations in the q space. The FT is not corrected for phase shifts.

also reveals four distinctive states associated with the peroxo-groups, namely the σ^*, π^*, π and σ from high to low energy, with the σ^* and π^* states lying respectively above and below the Fermi level (Fig. 6a). The positive Fukui function confirms the involvement of t_{2g}-like RuO* local level in oxidation (electron removal), but also shows the π^* oxygen states from

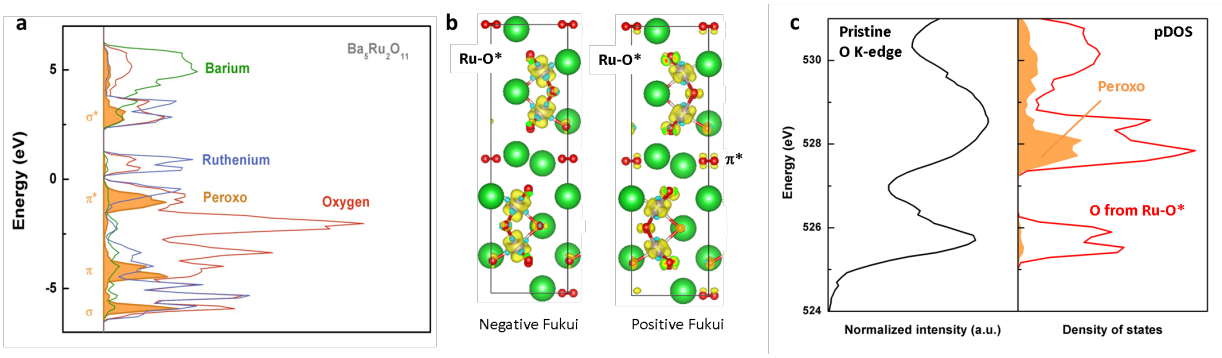

Figure 6: **a**. Atom-projected density of states (pDOS) computed from DFT for $Ba5Ru_2O_{11}$ where the oxide ions and ruthenium cations from the RuO_6 octahedra (red and blue, respectively) are differentiated from peroxide $(O_2)^{2-}$ groups in the Ba_2O_2 planes (plain orange). **b**. Negative and positive Fukui functions rendering the electronic density upon electron addition or removal, respectively, where Ru-O* orbitals are polarized upon reduction (negative Fukui) and Ru-O* as well as O-O π* states are polarized upon oxidation (positive Fukui). **c.** Comparison X-ray absorption measurement at the O K-edge for the pristine $Ba_5Ru_2O_{11}$ with the projected density of states for oxygen and peroxo-groups.

the peroxide groups to be polarized upon electron removal (Fig. 6b). From this computational study, several conclusions can already be drawn. First, O_2^{2-} peroxo-groups can potentially be oxidized which would eventually lead to the condensation of $O_{2(g)}$. Second, these peroxo-groups can hardly be reduced into O^{2-} due to the stabilization of the σ* states having a higher energy than the Ru-O antibonding t_{2g} states. This stabilization is critical since it will likely limit the reversibility of electrochemical reactions when the O_2^{2-}/O^{2-} redox couple is used as redox center for Li-ion battery materials or as OER redox active sites. Indeed, when the TM-O antibonding states lie between the π*-σ* gap for peroxo-groups, the electrochemical oxidation would affect the TM-O antibonding states prior to the σ* states from the peroxo-groups, following a linear response theory. Owing from the generally large π*-σ* gap for peroxo-groups (about 2.5 eV here and about 2 eV for Li_2O_2 for instance[43]), obtaining an active O_2^{2-}/O^{2-} redox couple in TM-based material is unfortunately

unlikely. To further support the computed DOS, XAS at the O K-edge was performed and compared with the DOS above the Fermi level (Fig. 6c). At around 526 eV, the first absorption peak can be assigned to the dipole transition from O(1s) states to the t_{2g}-like RuO* states with a predominant Ru character, as previously discussed. At higher energy ≈ 529 eV, a second and broader absorption peak can be observed. When compared to the computed DOS, this peak could be attributed to the overlap of two absorption peaks corresponding to the transitions O(1s) to RuO* states and O(1s) to O_2^{2-} σ* states. These spectra will be discussed later on in more detail.

To shine the light on the complex redox properties of these peroxo-groups, electrochemical measurements were then carried out. First, $Ba_5Ru_2O_{11}$ was used as an oxygen electrocatalyst in different aqueous media (Fig. 7). Under OER conditions at pH 13 (0.1 M KOH), a very limited electrocatalytic activity could be detected (dark blue in Fig. 7). While this observation is consistent with our previous observation that Ru^{5+}-containing perovskites La_2LiRuO_6 was not active in alkaline conditions,[6] it also indicates that the peroxo-groups are not active as redox center under these conditions. Ex situ atomic resolution HAADF-STEM imaging indicate that, aside from a slight amorphous surface, which is typical for hexagonal perovskites,[44] cycling under OER conditions at pH 13 doesn't induce drastic modifications in the bulk structure (Fig. S2). We thus decided to cycle the compound under reductive conditions at pH 13 (bottom part, dark blue in Fig. 7). Two successive reduction waves can be observed. The first reduction at about 0.3 V vs. NHE is associated with an oxidation peak (top blue curve in Fig. 7), presumably corresponding to the Ru^{5+}/Ru^{4+} redox couple balanced by the formation of oxygen defects. Interestingly, triggering this redox induces a large increase in the oxidation current above $E°(O_2/HO^-)$ (0.463 V vs. NHE at pH 13). Nevertheless, when pushing the electrochemical window to higher potential by decreasing the pH to 7 (top

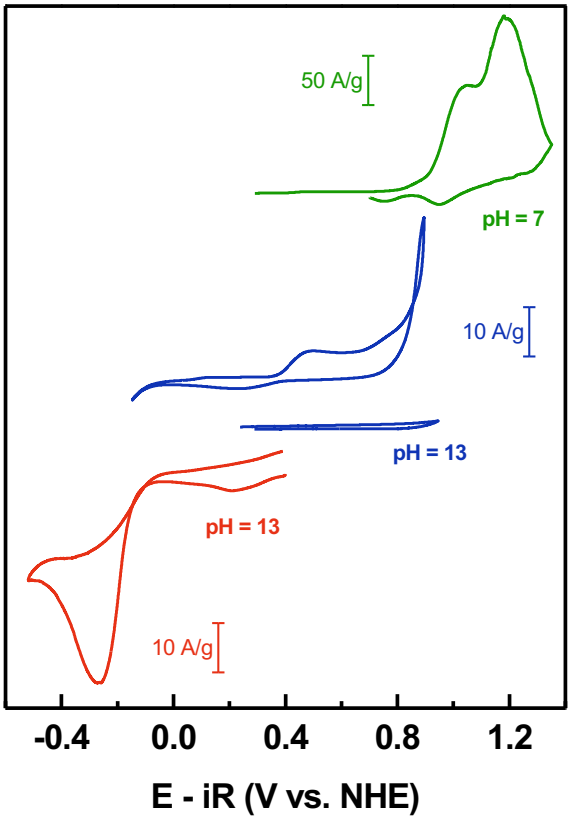

Figure 7: Aqueous electrochemistry of $Ba_5Ru_2O_{11}$ at different pH and under positive or negative polarization in argon-saturated solutions. E°(H_2O/O_2) at pH 13 is equal to 0.463 V vs. NHE and at pH 7 equal to 0.817 V vs. NHE.

curve, Fig. 7), two oxidation waves can be observed. Even though two corresponding reduction waves are observed in the backward scan, the drastic drop in current measured during the subsequent cycles (Fig. S3) as well as ex situ XRD measurement demonstrate the instability of the phase under such oxidizing conditions (Fig. S4). The decomposition is further confirmed by TEM data, which show that only a small portion of $Ba_5Ru_2O_{11}$ could be found in the sample after cycling at pH 7 (Fig. S2). All together, these observations rule out oxygen evolution from the oxidation of water as the sole origin for the oxidative current observed at pH 13. From the positive Fukui function discussed above, this oxidation process could be related to both the Ru^{6+}/Ru^{5+} and $O_{2(g)}/O_2^{2-}$ redox couples, these processes being

irreversible it is certainly detrimental for the stability of the phase. Going back to the reduction at pH 13, a second reduction wave can be observed at -0.2 V vs. NHE, potential at which the oxygen reduction reaction takes place. Similarly to the oxidation phenomenon, accessing the second reduction potential triggers instability of the phase, as seen in subsequent cycles.

To further unravel the complexity of these redox processes, $Ba_5Ru_2O_{11}$ was then cycled in aprotic electrolyte (1M $LiPF_6$ EC:DMC) where the behavior in oxidation was studied first (Fig. 8a). When oxidizing $Ba_5Ru_2O_{11}$ with no initial reaction with Li^+, a plateau at about 3.3 V vs. Li^+/Li is observed. When monitoring the gas pressure during this plateau (Fig. S5), an increase in pressure presumably owing to oxygen release, since the oxidation voltage is within the electrolyte stability window, could be observed. After reduction for a capacity corresponding to the reaction with 2 Li^+ (the behavior in reduction will be described in further details later on), a similar plateau could be observed with a relaxed potential of about 2.6 V vs. Li^+/Li (Fig. 8b). Therefore, this plateau is associated with the direct oxidation of $Ba_5Ru_2O_{11}$. The charge balance upon oxidation could presumably be achieved through the removal of Ba^{2+} cations together with the direct oxidation of lattice peroxide groups leading to the loss of $O_{2(g)}$. The aforementioned reaction could then be compared with the simple reaction $Ba^{2+} + O_{2(g)} + 2e^- = BaO_2$ ($\Delta G_{formation}$ = -578 kJ/mol at 298K) which would give a standard potential of about 3.12 V vs. Li^+/Li. This charge balance mechanism would be consistent with TEM data which demonstrate drastic structural instability triggered by this oxidation process (Fig. 9b), where the integrity of particles was found to be affected while leaving the crystal structure of the unaffected areas intact.

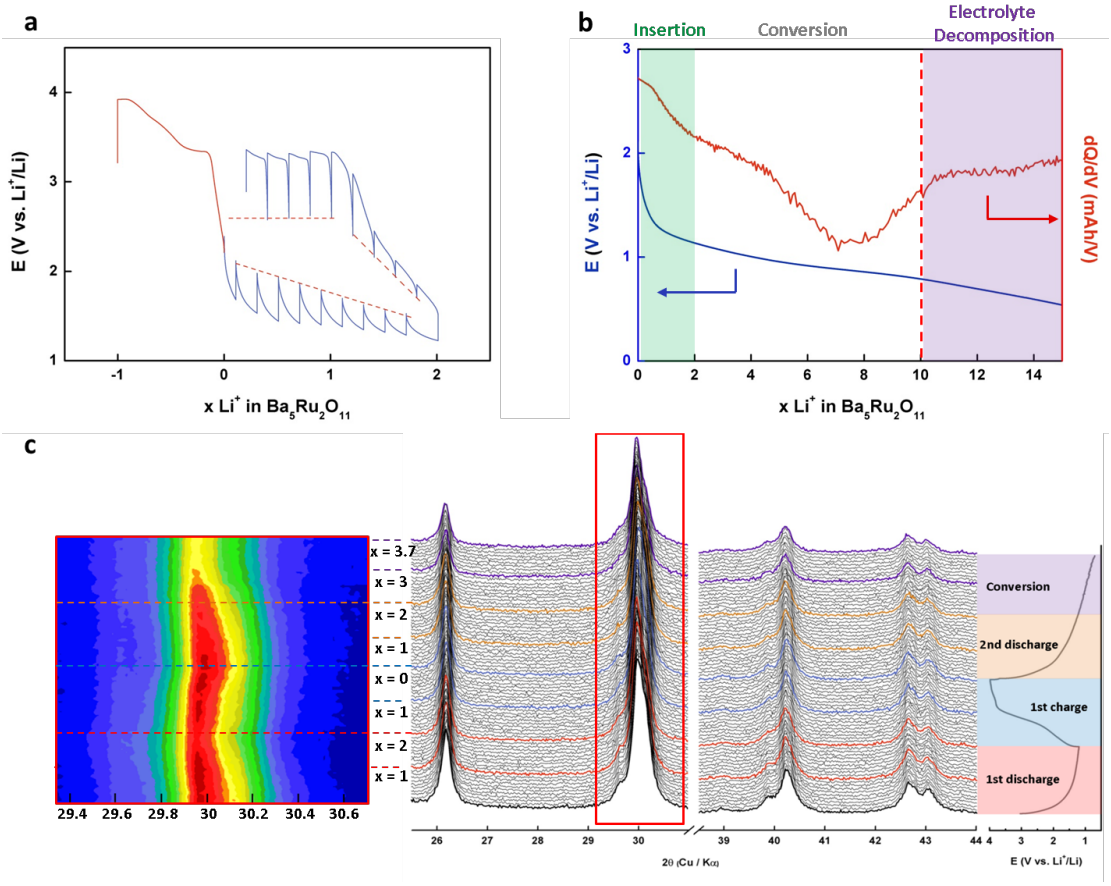

Figure 8: Electrochemistry of $Ba_5Ru_2O_{11}$ in organic electrolytes EC:DMC (1:1) 1M $LiPF_6$ with **a** a charge at C/10 (red) with no initial discharge compared to GITT curve with pulses corresponding to C/10 over 0.2 Li^+ followed by a 6 hours relaxation time in discharge and then charge (blue) and **b** a full discharge over 10 Li^+ corresponding to the full conversion into metallic ruthenium and and its corresponding derivative curve dQ/dV **c** In-situ XRD for $Ba_5Ru_2O_{11}$ in EC:DMC (1:1) 1M $LiPF_6$ with a first cycle starting in discharge over 2 Li^+ followed by a second discharge over 4 Li^+. A contour plot for the most intense peak at around 30° is provided on the left.

Turning back to the reactivity of $Ba_5Ru_2O_{11}$ with Li^+ in reduction, the galvanostatic discharge profile with a current density corresponding to C/5 (1 Li^+ exchanged in 5 hours) shows a sloping discharge from the OCV to the cut-off voltage (Fig. 8b). The derivative curve dQ/dV reveals that several processes take place during the reduction. Hence, before the large reduction peak observed for $2 \leq Li^+ \leq 10$ corresponding to the complete conversion of

$Ba_5Ru_2O_{11}$ into metallic Ru, a sloping behavior is observed. In situ XRD measurements were then carried out in the range $0 \leq Li^+ \leq 2$ to further understand this process (Fig. 8c). The measurements suggest that no drastic structural reorganization is encountered during the cycling of $Ba_5Ru_2O_{11}$ in this range, both in charge and in discharge. However, peak intensity was found to reversibly decrease while peaks position shifts. This behavior is in contrast with the drastic decrease in the peak intensity observed for $x > 2$ in discharge, which corresponds to the decomposition of the phase upon conversion. Hence, the electrochemical signature observed for $0 \leq Li^+ \leq 2$ could originate from either the reversible insertion of Li^+, as previously observed for bulk RuO_2,[45] or to the formation of Li_2O as previously observed for Bi-containing compounds.[46,47] Nevertheless, we could see that this reactivity with Li^+ leads to poor cyclability where only 1 Li^+ could be extracted back (Fig. 8a) and the cycling performances were found to quickly decrease (Fig. S6). Hence, high-resolution HAADF-STEM images were taken to better understand this reactivity (Fig. 9). Doing so, we could observe that the reactivity of $Ba_5Ru_2O_{11}$ with 2 Li^+ preserves the atomic arrangement of the material, but it results in pronounced corrugation of the structure layers. Apparently, this transformation is associated with the deformation of the Ba_2O_2 layers over few tens of nm on the outermost surface, which could indicate either small insertion of Li^+ or reduction of the Ba_2O_2 layers during the reactivity with Li^+ while the bulk remains unreacted (Fig. 9a).

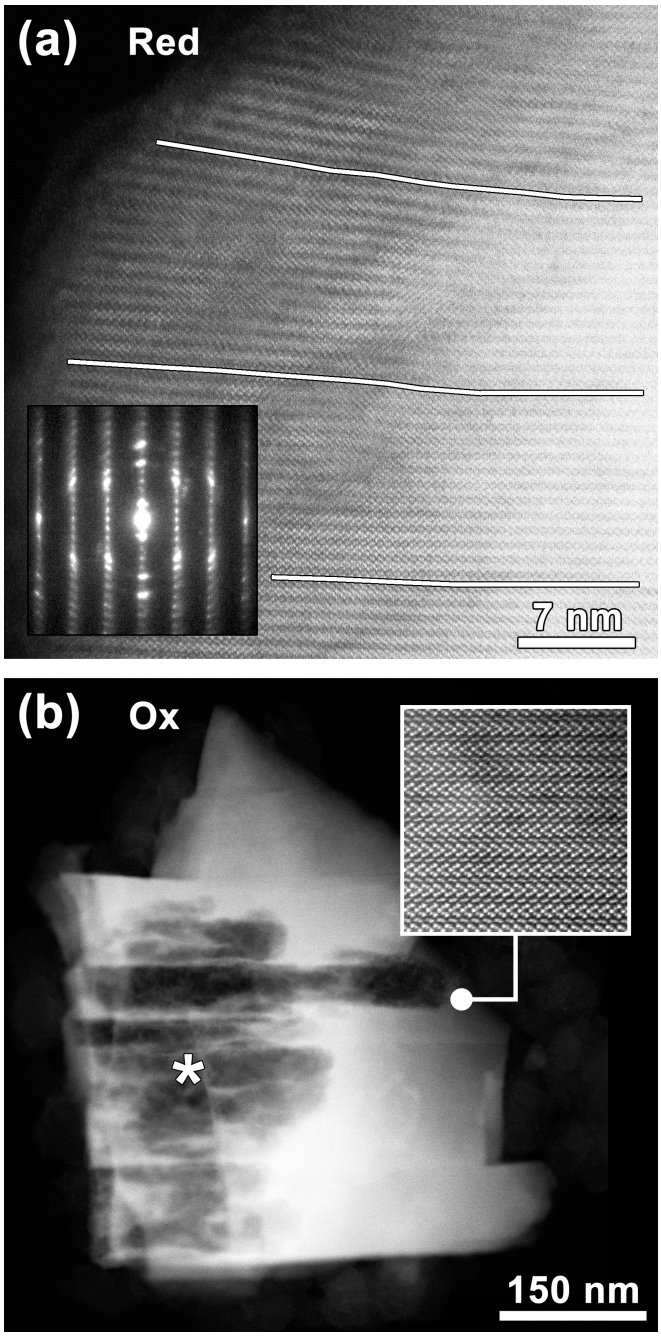

Figure 9: HAADF-STEM images taken along the [10$\bar{1}$0] zone axis of $Ba_5Ru_2O_{11}$ after electrochemical reduction (a) and oxidation (b) in non-aqueous medium. In image (a), lines highlight corrugation of the perovskite blocks due to swelling of the Ba_2O_2 layers; and the inset shows the corresponding ED pattern with characteristic tangential smering of the Bragg reflections. Image (b) is representative low magnification image. It demonstrates that a large portion of the particle is missing (marked with an asterisk); and the inset shows a high resolution HAADF-STEM image, confirming that the crystal structure of the material is preserved in the area unaffected by the dissolution.

The redox processes occurring upon reduction and oxidation for $Ba_5Ru_2O_{11}$ were further assessed by means of ex situ XAS measurements at the Ru K-edge and O K-edge (Fig. 10). First, the Ru K-edge was found to remain unchanged after direct oxidation of $Ba_5Ru_2O_{11}$ (Fig. 10a), consistent with our assumption that the oxidation is presumably counterbalanced by oxygen release and the phase dissolution, only leaving intact some part of the Ru^{5+}-containing pristine $Ba_5Ru_2O_{11}$ phase. Upon reduction, no shift in the Ru K-edge was observed after the reactivity with 1 Li^+, while a slight shift of the edge towards lower energy was observed after reactivity with 2 Li^+. This shift can be better seen when looking at the derivative of the normalized absorption (inset in Fig. 10a), and would indicate a slight reduction of Ru^{5+} upon reactivity with Li^+. Moreover, no significant modification in the EXAFS oscillations reflecting the bulk local structure was detected upon reduction (Fig. 10b). Overall, these observations highlight the limited reactivity of $Ba_5Ru_2O_{11}$ with Li^+ and therefore the limited reduction of the phase where only the top surface of particles was found reacted by TEM (Fig. 9). To further assess if the O_2^{2-}/O^{2-} redox couple is involved in reduction for the $Ba_5Ru_2O_{11}$ phase, XAS measurements at the O K-edge were performed in the bulk sensitive fluorescent yield (FY) mode (Fig. 10c). Looking at the O K-edge spectra recorded for the reduced and oxidized samples, two main peaks at 526 and 529 eV are observed. Upon cycling, the overall absorption intensity varies with a drastic drop of intensity measured in reduction. In details, the relative intensities for the peaks at 526 and 529 eV ascribed to the transition O(1s) to Ru-O* states and a combination of transition O(1s) to Ru-O* and O(1s) to peroxide σ* empty states, respectively, were found to vary concomitantly (Fig. 10d). This observation excludes the reduction of the peroxide groups which would only impact the peak at around 529 eV. Instead, it could be indicative of the accumulation of products formed on the surface upon reduction, as seen in the surface

sensitive total electron yield (TEY) mode (Fig. S7). Moreover, this would be in agreement with the negative Fukui function (Fig. 6b) where only the Ru-O* states were found to be polarized upon electron injection into $Ba_5Ru_2O_{11}$, as well as with the XAS measurements at the Ru K-edge where partial reduction of Ru^{5+} was observed (Fig. 10a). Overall, this study tend to confirm that the σ* O-O states formed for the peroxide groups are stabilized at too high energy and presumably don't participate to the reduction process.

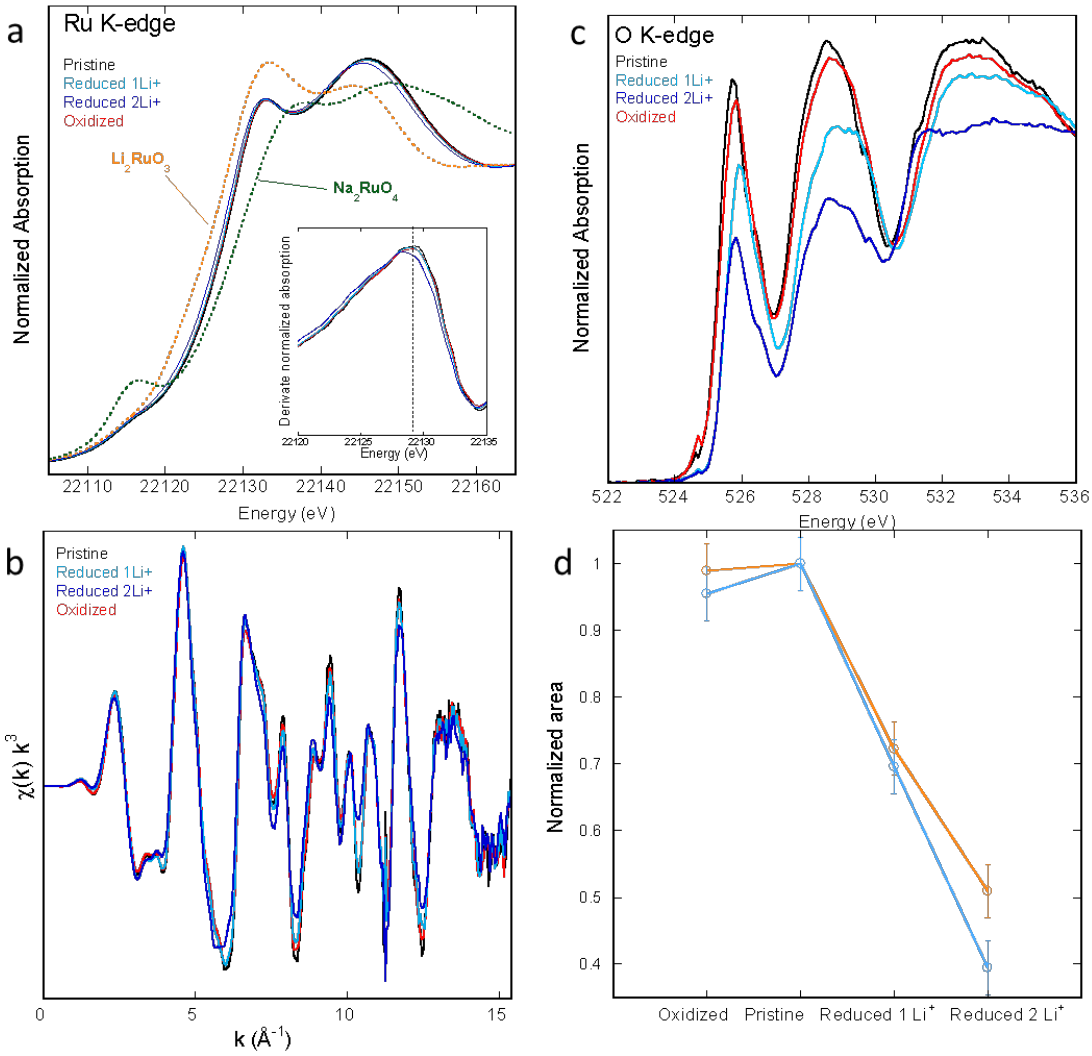

Figure 10: **a** Ru K-edge XANES spectra for pristine $Ba_5Ru_2O_{11}$ and the samples reduced with 1 Li^+, 2 Li^+ or oxidized for the equivalent of 1 Ba^{2+}. No significant differences in the edge position are observed as shown in the inset. In inset is shown the EXAFS oscillations weighted by k^3 of the pristine $Ba_5Ru_2O_{11}$ and ex situ samples. **b** O K-edge XAS spectra for pristine $Ba_5Ru_2O_{11}$ and ex situ samples compared to the atom-projected DOS for oxygen

states participating to Ru-O* states (red) and oxygen from peroxide groups (orange). **c** Evolution upon cycling of the integrated areas for the absorption peak at about 526 eV (orange) and about 529 eV (blue) normalized compared to the peaks for the pristine compound.

Discussion

In this study we could demonstrate that the stabilization of the peroxide $(O_2)^{2-}$ groups in the pristine transition metal oxide is detrimental for the redox activity of materials used as water oxidation catalysts or Li-ion battery positive electrodes. Indeed, when oxidizing lattice oxygen ions O^{2-} to form peroxide $(O_2)^{2-}$ groups during the charge of transition metal oxides used as positive electrode for Li-ion batteries, stabilization of the σ^* empty O-O states at high energy would occur. Therefore, these states lying well above the Fermi level become inactive upon reduction and are thus "frozen" inside the material which then follows a classical cationic redox reaction in reduction. Furthermore, the π^* O-O states that are formed within the peroxide groups lie just below the Fermi level and lead to an unstable situation upon charge where gaseous oxygen is presumably released. Owing to the bond order of the peroxide groups of one and its similar electronic configuration when compared to $O_{2(g)}$, the enthalpy required to release gaseous oxygen is therefore relatively positive and the potential for the redox couple O_2^{2-}/O_2 relatively low, ranging from 2.5 to 3.2 V vs Li^+/Li depending on the electrostatic interaction with the surrounding alkaline or alkaline-earth cations. Despite the relative ease to release gaseous oxygen which could be seen as a blessing for the oxygen evolution reaction, the cationic loss required to keep the charge balance is detrimental for the stability of the structure and one can already foresee catalysts proceeding through a direct lattice oxygen oxidation as prone to surface instability and drastic dissolution.[6,7,48,49] Therefore, two scenarios appear as preferential for Li-ion battery

materials and OER catalysts. For Li-ion battery positive electrodes, the reversible formation of peroxo-like $(O_2)^{n-}$ groups with a bond order lower than 1 and empty σ^* states lying just above the Fermi level appears as favorable when compared to the formation of true peroxide groups. Unfortunately, despite the strong appeal for such anionic redox behavior which allows for exchanging extra electrons and store more charge, slow kinetics in reduction[50] and surface instabilities for these groups are already foreseen.[24,26] For OER catalysts, the oxidation of lattice oxygen and the formation of oxyl $O^{\bullet-}$ radicals which would allow for a fast gaseous oxygen formation following an acid-base mechanism seems rather preferential, i.e. with the oxyl groups acting as electrophilic species while water acts as nucleophilic species. Indeed, it would be less destabilizing for the structure than a direct-coupling mechanism for which two oxidized lattice oxygen atoms form bond and eventually condensate to degas $O_{2(g)}$[22] which would imply the partial decoordination of transition metals as triggered by the increasing bond order between lattice oxygen ions. We could therefore demonstrate that peroxo-containing $Ba_5Ru_2O_{11}$ compound is unstable under OER conditions. Moreover, very little is known yet concerning the kinetics of these two mechanisms (acid-base and direct-coupling) and further work would be necessary in order to better understand them.

Conclusion

Using $Ba_5Ru_2O_{11}$ as a model compound, we could gain deeper insights into the redox behavior of peroxide groups in transition metal oxides used as OER catalysts and electrode for Li-ion batteries. Combining physical and electrochemical characterizations, we could demonstrate that the stabilization of the empty σ^* states of the peroxide group unfortunately freezes these states at high energy above the RuO* antibonding states and

thus the peroxide $(O_2)^{2-}$ cannot be reduced back to oxide ions. In oxidation, the peroxide groups which π^* states lie just below the Fermi level are redox active, leading to an unstable situation. This limitation eventually hampers the use of the O_2/O_2^{2-} redox couple and is in line with previous reports on the instability of high-valence iridium- and ruthenium-based oxides used as OER catalysts.[6,51–54] As a conclusion, peroxide groups as redox centers appear to be not favorable for OER catalysts and Li-ion battery materials owing to its bond order of 1 and the stabilization of its electronic states. More positively, this study calls for new chemical tricks to avoid the formation of such states when oxidizing transition metal oxides and to stabilize low bond order peroxo-like $(O_2)^{n-}$ groups with n being 3 (or O_3^{5-} groups, as described elsewhere[18,55]) for reversible Li-ion battery materials or highly reactive $O^{\bullet-}$ radicals with no lattice O-O bond formation for OER catalysts. No doubt that the importance of finding such compounds for the development of the next generation of energy storage devices will generate a lot of attention.

Methods

Materials synthesis and powder diffraction. $Ba_5Ru_2O_{11}$ was synthetized by hand grinding RuO_2 and $BaCO_3$ precursors followed by thermal treatment at 950°C for 48 hours under O_2. Laboratory X-ray diffraction (XRD) patterns were recorded with a Bruker D8 Advance diffractometer equipped with a copper source ($\lambda_{Cu\text{-}K\alpha1}$ = 1.54056 Å, $\lambda_{Cu\text{-}K\alpha2}$ = 1.54439 Å) and a LynxEye detector. Neutron powder diffraction (NPD) experiments were performed on the D1B powder diffractometer at the Institut Laue Langevin (Grenoble, France), with two wavelengths of 1.29 Å and 2.53 Å with the powder placed in a Ø=6mm cylindrical vanadium

can. The recorded patterns were refined using the Rietveld method as implemented in the FullProf program.[56–58]

Electrochemical measurements. Aqueous measurements were carried out by drop-casting an ink made by mixing tetrahydrofuran (THF; Sigma-Aldrich 99,9%) with $Ba_5Ru_2O_{11}$ powder and ethylene black carbon (Alfa Aesar 99,9%) in a 5:1 weight ratio as well as Nafion binder (5% weight, Ion Power). Note that for the measurements in alkaline solution, the Nafion was neutralized with KOH, whereas at neutral pH the Nafion was used as received. Glassy carbon electrodes with a surface of 0.196 cm^2 were used as support, with a loading of active material of 50 μg per electrode. Rotating disk electrode measurements were performed in glass cells previously cleaned by acid treatment following by boiling in water for 2 hours. A PINE Instrument device was used at 1600rpm. A solution of 0.1M KOH was used for pH = 13, while measurements in neutral pH a 0.1M H_2SO_4 solution was made into which 1 M KNO_3 was added to keep a high ionic strength and the solution adjusted to pH 7 by adding KOH pellets. All the measurements were carried out in Ar-saturated solutions. To prepare XRD and TEM samples, a high loading of 1 mg per electrode was used onto glassy carbon electrode with approximatively 1 cm^2 size. The powder was collected after washing with ethanol and sonication.

Electrochemical studies in organic solvent were carried out in Swagelock-type cells with a Li metal counter electrode and LP30 electrolyte (BASF) which were assembled in an argon-filled glovebox. The active material was ball milled with 10% carbon black (Super P, Timcal) using a SPEX ball mill for 20 minutes. For preparing XAS and TEM samples, powder was collected after cycling and washed with dimethyl carbonate and centrifuged before to be dried under vacuum.

Transmission electron microscopy.

Samples for transmission electron microscopy (TEM) were prepared by grinding materials in a mortar and dispersing the powder onto holey carbon TEM grids. Samples after electrochemical testing in non-aqueous solution were stored and prepared for TEM in argon environment; and a special Gatan Vacuum Transfer holder was used for analysis. High angle annular dark-field, annual bright field scanning TEM (HAADF-STEM and ABF-STEM, respectively) and ED patterns were acquired using a probe aberration corrected FEI Titan^3 80-300 electron microscope operated at 300 kV.

X-ray absorption spectroscopy.

XAS measurements at the Ru K-edge were performed in transmission mode at the ROCK beamline[59] of synchrotron SOLEIL (France). A Si (220) channel-cut quick-XAS monochromator with an energy resolution of 2 eV at 22 keV was used. The intensity of the monochromatic X-ray beam was measured with three consecutive ionization detectors. The samples were placed between the first and the second ionization chambers. For each measurement, successive spectra were collected at a rate of 2 Hz and averaged out over periods of 5 minutes. The energy calibration was established with simultaneous absorption measurements on RuO_2, placed between the second and the third ionization chambers. The data was treated using the Demeter package for energy calibration and normalization, and EXAFS oscillations were fitted using Artemis software.[60] Fourier transforms of EXAFS oscillations were carried out in k-range from 4.2 $Å^{-1}$ to 15.2 $Å^{-1}$. Fitting was performed in R-range from 1.0 to 2.9 Å using k^3 weight. EXAFS amplitudes and phase-shifts were calculated by FEFF7 starting from the calculated lattice parameters of the structures determined by combined Rietveld refinement of the neutron patterns. Except the radial distance (R) and

the Debye-Waller factor (σ^2), all other parameters were kept constant (N_i, E_0, S_0^2) in the conventional least squares modelling using the phase and amplitude factors calculated by the FEFF7. For ex situ XAS measurements, each cycled electrode was placed between two layers of Kapton tape, which was then sealed inside the argon glovebox within two layers of airtight transparent plastic pouches.

XAS spectra at O K-edge were collected on beamline 4-ID-C of the Advanced Photon Source (APS) at Argonne National Laboratory. The ex situ cathodes were transferred from an Ar-filled glovebox to the. Normalization of the XAS spectra as well as the fitting procedure were done using the Athena software.[60] The absorption step was reproduced using an error function. Gaussian curves were used to fit the peaks at 526 and 529 eV were used to fit the peak positions of the normalized XAS spectra.

First principle DFT calculations.

Spin-polarized density functional theory (DFT) calculations were performed using the plane-wave density functional theory VASP (Vienna ab initio simulation package) code[61,62] within the generalized gradient approximation of Perdew–Burke–Ernzerhof (PBE) to describe electron exchange and correlation.[63] The rotationally invariant Dudarev method[64] (DFT+U) was used to correct the self-interaction error of conventional DFT for correlated d-electrons. Crystal structures of the $Ba_5Ru_2O_{11}$ phase were shown to be well reproduced at Ueff = U − J = 2 eV for Ir (J = 1 eV). Conjugate gradient energy minimization procedure were used to relax all atom coordinates and lattice parameters until the forces acting on each atom were less than 1.10^{-3} eV/A. A plane-wave cutoff of 600 eV was used to describe the atomic basis set, with well-converged k-point sampling for each compound. Fukui functions have calculated

from charge density difference with phases where 0.4 % of the total number of electrons have been added or removed.

Acknowledgements

We thank S. Belin of the ROCK beamline (financed by the French National Research Agency (ANR) as a part of the "Investissements d'Avenir" program, reference: ANR-10- EQPX-45; proposal #20160095) of synchrotron SOLEIL for her assistance during XAS measurements. Authors would also like to thank V. Nassif for her assistance on the D1B beamline.

A.G, G.R. and J.-M.T acknowledge funding from the European Research Council (ERC) (FP/2014)/ERC Grant-Project 670116-ARPEMA.

References

(1) Cook, T. R.; Dogutan, D. K.; Reece, S. Y.; Surendranath, Y.; Teets, T. S.; Nocera, D. G. *Chem. Rev.* **2010**, *110*, 6474–6502.

(2) Larcher, D.; Tarascon, J.-M. *Nat. Chem.* **2015**, *7*, 19–29.

(3) Lewis, N. S.; Nocera, D. G. *Proc. Natl. Acad. Sci.* **2006**, *103* , 15729–15735.

(4) Grimaud, A.; Hong, W. T.; Shao-Horn, Y.; Tarascon, J.-M. *Nat. Mater.* **2016**, *15*, 121–126.

(5) Sathiya, M.; Rousse, G.; Ramesha, K.; Laisa, C. P.; Vezin, H.; Sougrati, M. T.; Doublet, M.-L.; Foix, D.; Gonbeau, D.; Walker, W.; Prakash, a S.; Ben Hassine, M.; Dupont, L.; Tarascon, J.-M. *Nat. Mater.* **2013**, *12*, 827–835.

(6) Grimaud, A.; Demortiere, A.; Saubanere, M.; Dachraoui, W.; Duchamp, M.; Doublet, M.; Tarascon, J. *Nat. Energy* **2017**, *2*, 16189.

(7) Grimaud, A.; Diaz-Morales, O.; Han, B.; Hong, W. T.; Lee, Y.-L.; Giordano, L.; Stoerzinger, K. a.; Koper, M. T. M.; Shao-Horn, Y. *Nat. Chem.* **2017**, *9*, 457–465.

(8) Pearce, P. E.; Perez, A. J.; Rousse, G.; Saubanère, M.; Batuk, D.; Foix, D.; Mccalla, E.; Abakumov, A. M.; Tendeloo, G. Van; Doublet, M.; Tarascon, J.-M. *Nat. Mater.* **2017**, *16*, 580–587.

(9) Saubanère, M.; McCalla, E.; Tarascon, J.-M.; Doublet, M.-L. *Energy Environ. Sci.* **2016**, *9*, 984–991.

(10) Xie, Y.; Saubanère, M.; Doublet, M.-L. *Energy Environ. Sci.* **2017**, *10*, 266–274.

(11) Seo, D.-H.; Lee, J.; Urban, A.; Malik, R.; Kang, S.; Ceder, G. *Nat. Chem.* **2016**, *8*, 692–697.

(12) Yabuuchi, N.; Nakayama, M.; Takeuchi, M.; Komaba, S.; Hashimoto, Y.; Mukai, T.; Shiiba, H.; Sato, K.; Kobayashi, Y.; Nakao, A.; Yonemura, M.; Yamanaka, K.; Mitsuhara, K.; Ohta, T. *Nat. Commun.* **2016**, *7*, 13814.

(13) Yabuuchi, N.; Takeuchi, M.; Nakayama, M.; Shiiba, H.; Ogawa, M.; Nakayama, K.; Ohta, T.; Endo, D.; Ozaki, T.; Inamasu, T.; Sato, K.; Komaba, S. *Proc. Natl. Acad. Sci. U. S. A.* **2015**, 1–6.

(14) Lee, E.; Persson, K. A. *Adv. Energy Mater.* **2014**, *4*, 1400498.

(15) Chen, H.; Islam, M. S. *Chem. Mater.* **2016**, *28*, 6656–6663.

(16) Cox, N.; Pantazis, D. A.; Neese, F.; Lubitz, W. *Acc. Chem. Res.* **2013**, *46*, 1588–1596.

(17) Cox, N.; Retegan, M.; Neese, F.; Pantazis, D. A.; Boussac, A.; Lubitz, W. *Science (80-.).* **2014**, *345*, 804–808.

(18) McCalla, E.; Abakumov, A. A.; Saubanere, M.; Foix, D.; Berg, E. J.; Rousse, G.; Gonbeau, D.; Novák, P.; van Tendeloo, G.; Dominko, R.; Tarascon, J.-M. *Science (80-.).* **2015**, *350*, 1516–1521.

(19) Siegbahn, P. E. M. *Proc. Natl. Acad. Sci.* **2017**, 5–7.

(20) Krewald, V.; Retegan, M.; Cox, N.; Messinger, J.; Lubitz, W.; Debeer, S.; Pantazis, D. A. *Chem. Sci.* **2015**, *6*, 1676–1695.

(21) Romain, S.; Bozoglian, F.; Sala, X.; Llobet, A. *J. Am. Chem. Soc.* **2009**, *131*, 2768–2769.

(22) Mavros, M. G.; Tsuchimochi, T.; Kowalczyk, T.; Mcisaac, A.; Wang, L.; Voorhis, T. Van. *Inorg. Chem.* **2014**, *53*, 6386–6397.

(23) Betley, T. A.; Wu, Q.; Voorhis, T. Van; Nocera, D. G. *Inorg. Chem.* **2008**, *47*, 1849–1861.

(24) Yabuuchi, N.; Yoshii, K.; Myung, S.; Nakai, I.; Komaba, S. *J. Am. Chem. Soc.* **2011**, *133*, 4404–4419.

(25) McCalla, E.; Sougrati, M. T.; Rousse, G.; Berg, E. J.; Abakumov, A.; Recham, N.; Ramesha, K.; Sathiya, M.; Dominko, R.; Van Tendeloo, G.; Novák, P.; Tarascon, J.-M. *J. Am. Chem. Soc.* **2015**, *137*, 4804–4814.

(26) Luo, K.; Roberts, M. R.; Hao, R.; Guerrini, N.; Pickup, D. M.; Liu, Y.-S.; Edström, K.; Guo, J.; Chadwick, A. V.; Duda, L. C.; Bruce, P. G. *Nat. Chem.* **2016**.

(27) Koga, H.; Croguennec, L.; Ménétrier, M.; Mannessiez, P.; Weill, F.; Delmas, C. *J. Power Sources* **2013**, *236*, 250–258.

(28) Assat, G.; Iadecola, A.; Delacourt, C.; Dedryvère, R.; Tarascon, J.-M. *Chem. Mater.* **2017**, *29*, 9714–9724.

(29) Bediako, D. K.; Costentin, C.; Jones, E. C.; Nocera, D. G.; Savéant, J.-M. *J. Am. Chem. Soc.* **2013**, *135*, 10492–10502.

(30) Surendranath, Y.; Kanan, M. W.; Nocera, D. G. *J. Am. Chem. Soc.* **2010**, *132*, 16501–16509.

(31) Fierro, S.; Nagel, T.; Baltruschat, H.; Comninellis, C. *Electrochem. commun.* **2007**, *9*, 1969–1974.

(32) Wohlfahrt-Mehrens, M.; Heitbaum, J. *J. Electroanal. Chem.* **1987**, *237*, 251–260.

(33) Mefford, J. T.; Rong, X.; Abakumov, A. M.; Hardin, W. G.; Dai, S.; Kolpak, A. M.; Johnston, K. P.; Stevenson, K. J. *Nat. Commun.* **2016**, *7*, 11053.

(34) Rong, X.; Parolin, J.; Kolpak, A. M. *ACS Catal.* **2016**, *6*, 1153–1158.

(35) Götzfried, T.; Reller, A.; Ebbinghaus, S. G. *Inorg. Chem.* **2005**, *44*, 6550–6557.

(36) Ebbinghaus, S. G.; Erztoument, C.; Marozau, I. *J. Solid State Chem.* **2007**, *180*, 3393–3400.

(37) Grasset, F.; Dussarrat, C.; Darriet, J.; Schweitzer, A. A. *J. Mater. Chem.* **1997**, *7*, 1911–1915.

(38) Grasset, F.; Zakhour, M.; Darriet, J. *J. Alloys Compd.* **1999**, *287*, 25–31.

(39) Findlay, S. D.; Shibata, N.; Sawada, H.; Okunishi, E.; Kondo, Y.; Ikuhara, Y. *Ultramicroscopy* **2010**, *110*, 903–923.

(40) Jacquet, Q.; Perez, A.; Batuk, D.; Tendeloo, G. Van; Rousse, G.; Tarascon, J. *Chem. Mater.* **2017**, *29*, 5331–5343.

(41) Montemore, M. M.; Spronsen, M. A. Van; Madix, R. J.; Friend, C. M. *Chem. Rev.* **2017**.

(42) Sathiya, M.; Rousse, G.; Ramesha, K.; Laisa, C. P.; Vezin, H.; Sougrati, M. T.; Doublet, M.-L.; Foix, D.; Gonbeau, D.; Walker, W.; Prakash, a S.; Ben Hassine, M.; Dupont, L.; Tarascon, J.-M. *Nat. Mater.* **2013**, *12*, 827–835.

(43) Viswanathan, V.; Thygesen, K. S.; Hummelshøj, J. S.; Norskov, J. K.; Girishkumar, G.; Mccloskey, B. D.; Luntz, A. C. *J. Chem. Phys.* **2011**, *135*, 214704.

(44) Grimaud, A.; Carlton, C. E.; Risch, M.; Hong, W. T.; May, K. J.; Shao-horn, Y. *J. Phys. Chem. C* **2013**, *117*, 25926–25932.

(45) Delmer, B. O.; Balaya, P.; Kienle, L.; Maier, J. *Adv. Mater.* **2008**, *20*, 501–505.

(46) Patoux, S.; Vannier, R.-N.; Mairesse, G.; Nowogrocki, G.; Tarascon, J. *Chem. Mater.* **2001**, *13*, 500–507.

(47) Strauss, F.; Rousse, G.; Batuk, D.; Tang, M.; Salager, E.; Draz, G.; Dominko, R.; Tarascon, J. *Phys. Chem. Chem. Phys.* **2018**, *20*, 2330–2338.

(48) Yang, C.; Grimaud, A. *Catalysts* **2017**, *7*, 149.

(49) Grimaud, A.; May, K. J.; Carlton, C. E.; Lee, Y.-L.; Risch, M.; Hong, W. T.; Zhou, J.; Shao-Horn, Y. *Nat. Commun.* **2013**, *4*, 2439.

(50) Assat, G.; Delacourt, C.; Alves Dalla Corte, D.; Tarascon, J. *J. Electrochem. Soc.* **2016**, *163*, A2965–A2976.

(51) Chang, S. H.; Danilovic, N.; Chang, K.-C.; Subbaraman, R.; Paulikas, A. P.; Fong, D. D.; Highland, M. J.; Baldo, P. M.; Stamenkovic, V. R.; Freeland, J. W.; Eastman, J. a; Markovic, N. M. *Nat. Commun.* **2014**, *5*, 4191.

(52) Cherevko, S.; Geiger, S.; Kasian, O.; Kulyk, N.; Grote, J.-P.; Savan, A.; Shrestha, B. R.; Merzlikin, S.; Breitbach, B.; Ludwig, A.; Mayrhofer, K. J. J. *Catal. Today* **2016**, *262*, 170–180.

(53) Cherevko, S.; Zeradjanin, A. R.; Topalov, A. a.; Kulyk, N.; Katsounaros, I.; Mayrhofer, K. J. J. *ChemCatChem* **2014**, *6*, 2219–2223.

(54) Kasian, O.; Grote, J.; Geiger, S.; Cherevko, S.; Mayrhofer, K. J. J. *Angew. Chem. Int. Ed. Engl.* **2018**, *57*, 2488–2491.

(55) Demourgues, A.; Weill, A.; Darriet, B.; Wattiaux, A.; Grenier, J.-C.; Gravereau, P.; Pouchard, M. *J. Solid State Chem.* **1993**, *106*, 330–338.

(56) Rietveld, H. M. *J. Appl. Crystallogr.* **1969**, *2*, 65–71.

(57) Rodriguez-carvajal, J. *Phys. B Condens. Matter* **1993**, *192*, 55–69.

(58) FullProf Suite.

(59) Briois, V.; La Fontaine, C.; Belin, S.; Barthe, L.; Moreno, T.; Pinty, V.; Carcy, A.; Girardot, R.; Fonda, E. *J. Phys. Conf. Ser.* **2016**, *712*, 012149.

(60) Ravel, B.; Newville, M. *J. Synchrotron Radiat.* **2005**, *12*, 537–541.